Journal of Biomechanics 60 (2017) 203–210

Contents lists available at ScienceDirect

Journal of Biomechanics

journal homepage: www.elsevier.com/locate/jbiomech
www.JBiomech.com

On estimating intraventricular hemodynamic forces from endocardial dynamics: A comparative study with 4D flow MRI

Gianni Pedrizzetti [a,*], Per M. Arvidsson [b], Johannes Töger [b], Rasmus Borgquist [c], Federico Domenichini [d], Håkan Arheden [b], Einar Heiberg [c,e]

[a] Department of Engineering and Architecture, University of Trieste, Trieste, Italy
[b] Lund University, Skane University Hospital, Department of Clinical Sciences, Clinical Physiology, Lund, Sweden
[c] Lund University, Skane University Hospital, Department of Arrhythmias, Lund, Sweden
[d] Department of Civil and Environmental Engineering, University of Firenze, Firenze, Italy
[e] Department of Biomedical Engineering, Lund University, Lund, Sweden

ARTICLE INFO

Article history:
Accepted 25 June 2017

Keywords:
Cardiac fluid dynamics
Hemodynamic forces
Intraventricular pressure gradient
4D flow MRI

ABSTRACT

Intraventricular pressure gradients or hemodynamic forces, which are their global measure integrated over the left ventricular volume, have a fundamental importance in ventricular function. They may help revealing a sub-optimal cardiac function that is not evident in terms of tissue motion, which is naturally heterogeneous and variable, and can influence cardiac adaptation. However, hemodynamic forces are not utilized in clinical cardiology due to the unavailability of simple non-invasive measurement tools.

Hemodynamic forces depend on the intraventricular flow; nevertheless, most of them are imputable to the dynamics of the endocardial flow boundary and to the exchange of momentum across the mitral and aortic orifices. In this study, we introduce a simplified model based on first principles of fluid dynamics that allows estimating hemodynamic forces without knowing the velocity field inside the LV.

The model is validated with 3D phase-contrast MRI (known as 4D flow MRI) in 15 subjects, (5 healthy and 10 patients) using the endocardial surface reconstructed from the three standard long-axis projections. Results demonstrate that the model provides consistent estimates for the base-apex component (mean correlation coefficient $r = 0.77$ for instantaneous values and $r = 0.88$ for root mean square) and good estimates of the inferolateral-anteroseptal component ($r = 0.50$ and 0.84, respectively).

The present method represents a potential integration to the existing ones quantifying endocardial deformation in MRI and echocardiography to add a physics-based estimation of the corresponding hemodynamic forces. These could help the clinician to early detect sub-clinical diseases and differentiate between different cardiac dysfunctional states.

1. Introduction

Heart function is about creating and sustaining blood motion (Richter and Edelman, 2006) through a proper contraction-relaxation timing of the myocardial muscle. Recent advances in cardiac mechanics were primarily founded on the assessment of myocardial deformation (Shah and Solomon, 2012). Echocardiography and cardiac magnetic resonance imaging (MRI) have permitted valuable clinical contributions to the non-invasive diagnosis of cardiac dysfunctions based on myocardial deformation (Claus et al., 2015). However, every heart is different and the variability in geometry and local curvature of the left ventricle (LV) entails different amplitude and timing of regional motion (Bogaert and Rademakers, 2001; Maffessanti et al., 2011). Different normal patterns of LV regional deformation allow a natural synchrony, which does not mean simultaneity, able to create the proper intraventricular pressure gradients (IVPGs) that drive blood motion during both ventricular ejection and ventricular filling. The absence of a unique, normal space-time deformation pattern introduces potential ambiguity in the assessment of early abnormalities. Differently, from the perspective of blood flow, an incorrect sequence of IVPGs and their deviation from the base-apex direction represent unequivocal indications of suboptimal function. Therefore, it may be advantageous to provide methods for assessment of IVPGs themselves.

* Corresponding author at: Department of Engineering and Architecture, University of Trieste, P.le Europa 1, 34127 Trieste, Italy.
E-mail address: giannip@dia.units.it (G. Pedrizzetti).

http://dx.doi.org/10.1016/j.jbiomech.2017.06.046
0021-9290/

Clinical studies about base-apex IVPGs were based on catheterization in animal models (Courtois et al., 1988) and sometimes on the post-processing of color Doppler M-mode echocardiography (Firstenberg et al., 2000; Tonti et al., 2001). Available results showed that IVPGs reach a maximum value, directed from base to apex, at the transition between systole and diastole; this dynamic actions corresponds to the deceleration of the systolic ejection and the later thrust to LV filling; conversely, pressure pushes from apex to base at late diastole preparing the systolic ejection. This dynamic rhythm is a clear marker of normal function that is altered in either systolic or diastolic dysfunctions and abolished during heart failure (Guerra et al., 2013b). Despite their apparent importance, IVPGs have been rarely utilized in clinical cardiology due to the complexity of their acquisition.

Advancements in echocardiography and MRI allow the measurement of blood flow field inside the left ventricle (LV) and, from post-processing, the calculation of the corresponding pressure field (Ebbers et al., 2001; Cimino et al., 2012). The concept of hemodynamic forces was then introduced as a mathematically well-defined global measure which corresponds to the integrated IVPGs inside the LV and represents the force exchanged between the blood and the surrounding tissue (Pedrizzetti et al., 2015). In echocardiography, clinical studies based on a dedicated particle image velocimetry technique (Echo-PIV) demonstrated that hemodynamic forces are modified by alteration of LV synchrony, suggesting their potential ability to predict remodeling in patients undergoing cardiac resynchronization therapy (Pedrizzetti et al., 2016). The application of Echo-PIV requires injection of contrast agent and high quality images recorded at high frame rate: a procedure that is not routinely feasible and that requires specific expertise.

Phase-contrast MRI (PC-MRI) represents the reference standard for measuring blood velocities in the heart and large vessels, although it requires valuable equipment and competence that limit its routine clinical use. Three-dimensional (3D) PC-MRI (often referred as 4D flow MRI) was used to evaluate hemodynamic forces in the LV on both normal and diseased subjects (Arvidsson et al., 2016b; Eriksson et al., 2016). PC-MRI force measurements were highly reproducible (Töger et al., 2016) and demonstrated a consistent pattern in normal subjects, where forces are directed along the LV axis, which is noticeably altered in dilated and dysfunctional hearts.

Hemodynamic forces, or equivalently IVPGs, depend on the details of intraventricular flow; nevertheless, a large part of them can be imputable to the gross flow properties that follow from the motion of the LV tissue and from the exchange of momentum across the mitral and aortic orifices. The aim of this study is that of introducing and validating a simplified low-dimensional model based on global balances in fluid dynamics that allows estimating the main features of the hemodynamic force vector from the dynamics of the endocardial tissue, not requiring knowledge of the velocity field inside the LV. This model is an extension and revision of one previously presented in a theoretical context with a truncated prolate spheroid geometry (Domenichini and Pedrizzetti, 2016). The model is subjected to validation by comparison with results obtained by 4D flow MRI in a set of very heterogeneous subjects to assess its reliability and limitations.

2. Methods I: Clinical MR imaging

This study includes 3 healthy volunteers, 2 elite endurance athlete and 10 patients with heart failure in NYHA class ranging from II to IV. All normal subjects were originally included in a previously published study (Arvidsson et al., 2016b). Cases were selected by one of the authors (PA) to represent a wide range of cardiac dimensions, both in health and disease, with the objective of testing the model under variable conditions, although with no aim of drawing any clinical conclusion. The study was performed in accordance with the Helsinki declaration; all subjects provided written informed consent.

MRI acquisition and quantification procedure was previously described (Arvidsson et al., 2016b; Kanski et al., 2015) and is briefly summarized here. All subjects underwent cardiovascular magnetic resonance imaging on a 1.5 T Philips Achieva (Philips, Best, The Netherlands), including balanced steady-state free precession (bSSFP) cine images in standard short- and long-axis projections and four-dimensional (4D = 3D + time) flow measurements by PC-MRI covering the whole heart. Retrospective ECG gating was used for both bSSFP and 4D flow imaging. The spatial resolution of bSSFP was 1.3 × 1.3 mm in-plane with 8.0 mm slice thickness, acquired temporal resolution was 30 ms and the acquired data reconstructed to 30 timeframes per heartbeat; differently, the resolution of 4D flow measurements was 3 mm isotropic, acquired temporal resolution 50 ms, reconstructed to 40 timeframes per heartbeat.

To define the LV cavity for subsequent quantification of hemodynamic forces, the endocardial borders were delineated on each short-axis slice in all timeframes over the cardiac cycle, using the image analysis software Segment 2.0 (Medviso, Lund, Sweden) (Heiberg et al., 2010; Tufvesson et al., 2015). Then, the global hemodynamic force vector was evaluated by computing the integral balance of momentum

$$\boldsymbol{F}(t) = \int_{V(t)} \rho \left(\frac{\partial \boldsymbol{v}}{\partial t} + \boldsymbol{v} \cdot \nabla \boldsymbol{v} \right) dV, \tag{1}$$

where $V(t)$ indicates the 3D LV flow domain and the integral is computed as the sum of values on each slice multiplied by the slice thickness; $\boldsymbol{v}(\boldsymbol{x}, t)$ is the velocity vector field measured with PC-MRI and ρ is the blood density (Arvidsson et al., 2016b). The cross-sectional area of the aorta was measured using a separate 2D PC-MR flow acquisition in a plane perpendicular to the vessel in the proximal ascending aorta. Mitral inflow area was estimated by measuring the smallest cross-sectional area (vena contracta) of the E-wave inflow profile during peak early diastolic filling, using the 4D flow data (Arvidsson et al., 2016a). Measurement methods were previously described and figures are in line with existing reference values (Carlsson et al., 2012; Kawel-Boehm et al., 2015; Steding et al., 2010). Table 1 reports the main cardiac parameters relevant to this study.

The LV cavity is also delineated separately on the long-axis projections for usage in the mathematical model. The endocardial border is segmented in each long axis projection in all timeframes with the same image analysis software; the three long axis endocardial borders are provided as input to the model.

3. Methods II: Mathematical model

The input data used by the model consists of the three long-axis LV borders at all MRI timeframes and the average valve areas.

The LV endocardial surface is reconstructed from the long-axis borders corresponding to the 2-, 3- and 4-chamber projections. To this purpose the LV axis on each projection is computed as the line connecting the center of the base with the apex, defined as the farther point. The three borders are combined by overlapping the three LV axis and considering a relative rotation by 60° using anatomical landmark on each slice to ensure correct circumferential sequence. The entire LV endocardial surface is then described by its 3D coordinates evaluated by interpolation on a structured mesh made of 36 points along the circumference and 32 points from base to apex; however, results were independent from the specific number of interpolation points. Volumes computed in this tri-plane simplified geometry resulted a little underestimated with respect to the complete 3D method, mainly because part of the higher outflow tract and sub-mitral volumes were cut away. Linear correlation showed that tri-plane end-systolic and end-diastolic volumes were 0.90 × ESV and 0.91 × EDV with correlation coefficient 0.999 and 0.997, respectively. The reconstructed endocardial boundary, shown in Fig. 1 for one normal case, is used for modeling the LV flow.

The two terms inside the integral (1) represent the inertial and convective terms, respectively. They can be rewritten expressing the second term as momentum flux at the boundaries

$$\boldsymbol{F}(t) = \int_{V(t)} \rho \frac{\partial \boldsymbol{v}}{\partial t} dV + \int_{S(t)} \rho \boldsymbol{v} (\boldsymbol{v} \cdot \boldsymbol{n}) dS = \boldsymbol{I}(t) + \boldsymbol{M}(t), \tag{2}$$

where $S(t)$ is the boundary surface of the fluid domain, $V(t)$, and $\boldsymbol{n}$ is the outward unit normal vector. The two terms are synthetically indicated by the symbols $\boldsymbol{I}(t)$ and $\boldsymbol{M}(t)$. We outline below a method to estimate the integrals in (2) from global properties in absence of the knowledge of the velocity field inside the LV. The present model represents a revision of what previously introduced in a theoretical context (Domenichini and Pedrizzetti, 2016) with important improvements to ensure its general validity and to allow application to diagnostic imaging.

Consider Cartesian coordinates with the z-axis directed from the LV apex (set at $z = 0$) to the center of the LV basal surface, the x-axis directed from the center of aortic outflow to that of the mitral orifice, i.e. from the anteroseptal to the inferolateral wall, and the y-axis perpendicular in a right-hand set. The z-coordinate ranges from 0 to the LV height $H(t)$ and $A(z, t)$ indicates the transversal LV area at each level z such that the ventricular volume is

Table 1
Main clinical characteristics of the enrolled subjects.

#		EDV [cm^3]	ESV [cm^3]	EF [%]	NYHA Class	HR_{SSFP} [bpm]	HR_{4DFlow} [bpm]	A_{mv} [cm^2]	A_{ao} [cm^2]
1	Normal #1	170	56	67	–	60	58	7.23	5.43
2	Normal #2	151	62	59	–	68	70	10.15	5.13
3	Normal #3	133	56	58	–	53	54	6.85	4.75
4	Athlete #1	218	81	63	–	53	60	8.19	8.04
5	Athlete #2	289	139	52	–	38	38	14.29	5.65
6	Patient #1	383	238	38	III	59	67	9.21	8.85
7	Patient #2	168	96	43	II	54	58	6.91	6.65
8	Patient #3	743	665	10	II	83	76	12.06	5.75
9	Patient #4	274	192	30	IV	49	58	7.96	10.91
10	Patient #5	285	189	34	III	52	55	6.11	7.84
11	Patient #6	330	246	25	III	79	76	9.87	8.05
12	Patient #7	181	122	32	II	79	72	9.80	11.13
13	Patient #8	394	315	20	IV	60	58	5.56	7.67
14	Patient #9	376	270	28	II	68	66	8.18	8.97
15	Patient #10	174	101	42	3III	72	65	8.81	10.36

EDV = End-Diastolic Volume; ESV = End-Systolic Volume; EF = Ejection Fraction; HR = Heart Rate; A_{mv} = Mitral inflow Area; A_{ao} = Aortic Area.

$$V(t) = \int_0^{H(t)} A(z,t)dz. \tag{3}$$

The inertial term on the right hand side of (2) can be computed exactly as

$$\boldsymbol{I}(t) = \rho V(t)\frac{d\boldsymbol{U}(t)}{dt}; \tag{4}$$

where $\boldsymbol{U}(t)$ is the velocity vector averaged in the entire LV cavity whose estimation allows one for $\boldsymbol{I}(t)$. For the z-component we can write, at each level z, the balance of mass

$$\frac{d}{dz}(V_z(z,t)A(z,t)) = -\frac{dA(z,t)}{dt}, \tag{5}$$

where $V_z(z,t)$ is the average velocity at level z. Eq. (5) can be immediately integrated to provide the z-component of the LV-averaged velocity to be inserted in (4)

$$U_z(t) = \frac{1}{V(t)}\int_0^{H(t)}\left\{\int_0^z -\frac{dA(s,t)}{dt}ds\right\}dz. \tag{6}$$

The x-component of the LV averaged velocity is due to the transfer of momentum along x from the mitral inflow to the outflow tract. The average longitudinal velocity, $V_z(z,t)$, that appears in (5) is associated to a purely radial velocity on the transversal plane,

$$V_r = -\frac{r}{2}\frac{dV_z}{dz}, \tag{7}$$

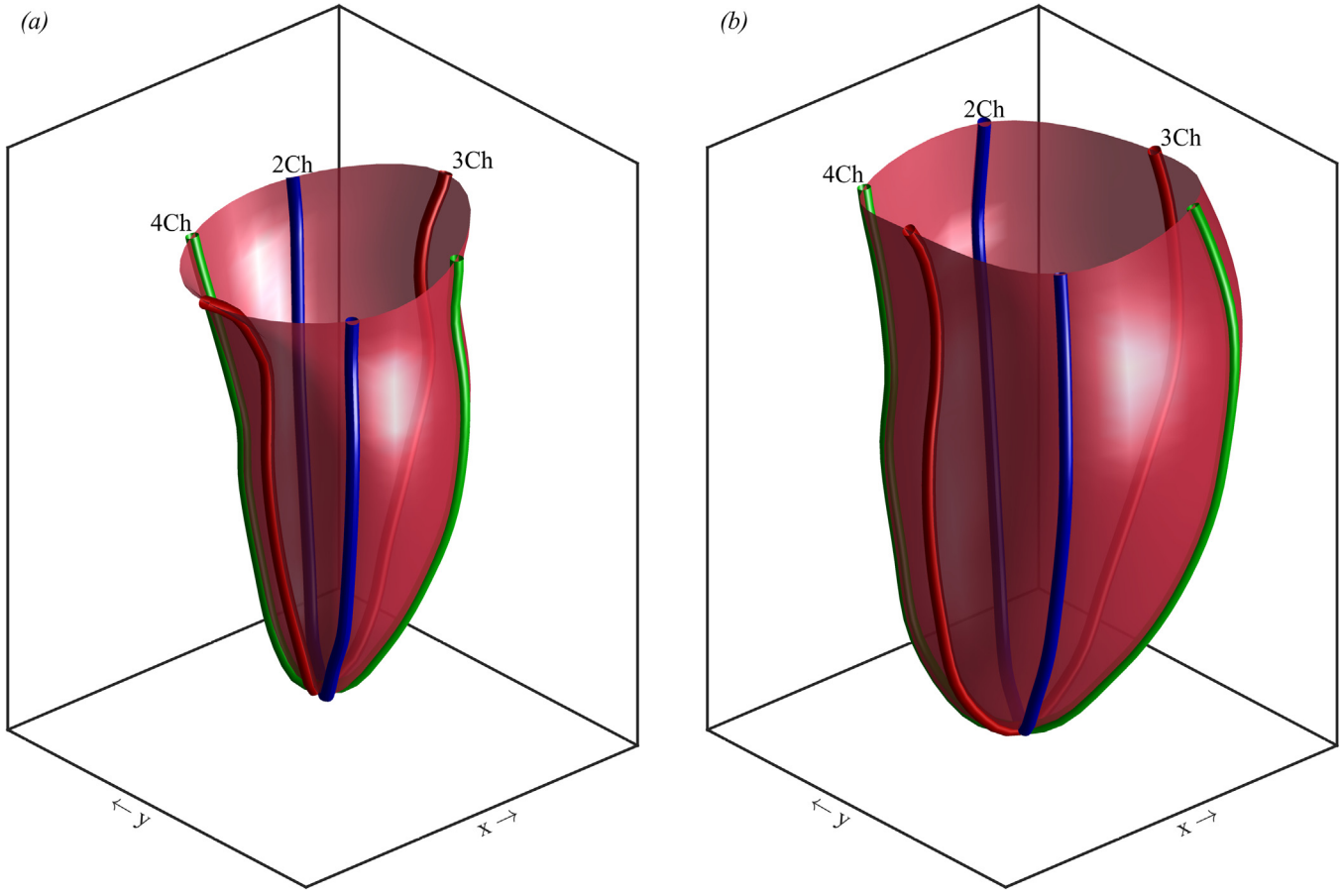

Fig. 1. Left ventricle endocardial boundary, for one normal case, reconstructed from the three long axis borders (2-, 3- and 4-Chambers); (a) end systolic and (b) end-diastolic endocardial surfaces are shown with indication of the corresponding long axis borders.

that has no average component along x. For estimating a mean transversal motion, assume that the inflow/outflow fluid velocity is predominantly oriented along the z-direction and approximately symmetric with respect to the xz-plane. This is probably the main limitation of the model that does not account for the deviation of the inflow that may occur in presence of valvular anomalies, an effect that could especially influence the y-component of the force. Under this assumption, for the sake of evaluating balances averaged over the cross section, the vertical velocity is expressed as the sum of its mean value $V_z(z,t)$ and an asymmetric component $V_z^{(1)}(z,\vartheta,t)$ such that $v_z(x,y,z,t) \approx V_z(z,t) + V_z^{(1)}(z,\vartheta,t)$, where ϑ is the circumferential coordinate, defined by $x = r\cos\vartheta, y = r\sin\vartheta$ with $r = \sqrt{x^2+y^2}$. We choose $V_z^{(1)}(z,\vartheta,t) = v_z^{(1)}(z,t)\cos\vartheta$, using the function $\cos\vartheta$ as asymmetry-weighting function. The choice of the simple co-sinusoidal function allows an easier analytical manipulation, nevertheless other options could be considered.

The conservation of mass can be recast in terms of asymmetric components only

$$\frac{\partial V_x^{(1)}}{\partial x} + \frac{\partial V_y^{(1)}}{\partial y} = -\frac{d v_z^{(1)}}{dz}\cos\vartheta; \tag{8}$$

where the superscript (1) is used to indicate all components associated with the non-symmetric velocity $V_z^{(1)}$. The simplest in-plane velocity field that satisfies (8) is

$$\begin{aligned} V_x^{(1)}(r,\theta,z) &= \left(\tfrac{2}{3}R - \tfrac{1}{2}r - \tfrac{1}{6}r\cos 2\vartheta\right)\tfrac{dv_z^{(1)}}{dz}; \\ V_y^{(1)}(r,\theta,z) &= -\tfrac{r}{6}\sin 2\vartheta\,\tfrac{dv_z^{(1)}}{dz}. \end{aligned} \tag{9}$$

The specific solution (9) included the integration constant to have zero radial velocity at the boundary, assumed approximately circular of radius $R(z,t) = \frac{3}{2A}\int_A r dA$, while a possible net boundary motion is accounted separately below. Solution (9) also included the additional constraint that this velocity is irrotational to avoid appearance of spurious vorticity from arguments based on mass balance only. To better exemplify this point, the velocity field (9) is shown in Fig. 2a; its combination with a (arbitrary) positive radial flow corresponding to diastole and a negative radial flow in systole are shown in Fig. 2b and c, respectively.

Integrating (9) over the cross-section and along the LV axis allows estimating the x-component of the velocity averaged in the LV

$$U_x(z,t) = \frac{1}{3V(t)}\int_0^{H(t)} A(z,t)R(z,t)\frac{dv_z^{(1)}}{dz}dz + \frac{1}{V(t)}\int_0^{H(t)} V_{xw}(z,t)A(z,t)dz; \tag{10}$$

the last term in (10) was added to account for the possible net translation of the LV boundary where $\boldsymbol{V}_w(z,t)$ is the average velocity of the LV boundary at level z.

Formula (10) requires the evaluation of the term $\frac{dv_z^{(1)}}{dz}$. Assume the simplest case of a linear decrease of the flux, from the basal profile to the null value at the apex, writing a relation formally analogous to (5)

$$\frac{d}{dz}\left(v_z^{(1)}A(z,t)\right) = \frac{v_z^{(1)}(H)A(H)}{H(t)}, \tag{11}$$

from which

$$\frac{dv_z^{(1)}}{dz}(t) = v_z^{(1)}(H,t)\frac{A(H,t)}{H(t)}\frac{d}{dz}\left(\frac{z}{A(z,t)}\right) = \frac{v_z^{(1)}(H,t)}{H(t)}\frac{A(H,t)}{A(z,t)}\left(1 - \frac{z}{A(z,t)}\frac{dA}{dz}\right), \tag{12}$$

Introduction of (12) into (10) gives the estimate of the x-component of the velocity averaged in the LV

$$\begin{aligned} U_x(t) = \frac{1}{3V(t)}v_z^{(1)}(H)\frac{A(H)}{H(t)}\int_0^{H(t)} R(z,t)\left(1 - \frac{z}{A(z,t)}\frac{dA}{dz}\right)dz + \frac{1}{V(t)} \\ \times \int_0^{H(t)} V_{xw}(z,t)A(z,t)dz. \end{aligned} \tag{13}$$

This equation requires only the knowledge of the asymmetric velocity at the basal level, $z = H$, at every instant. Both the average velocity V_z and the asymmetric component $V_z^{(1)}$ at the LV base can be obtained by measurements of inflow and outflow. When such level of detail is not available, these can be estimated crudely as

$$\begin{aligned} V_z(H(t),t) &= \tfrac{dH}{dt} - \tfrac{1}{A(H)}\tfrac{dV(t)}{dt}; \\ v_z^{(1)}(H(t),t) &\approx \begin{cases} \frac{-1}{2A_{mv}}\frac{dV(t)}{dt}, & \frac{dV(t)}{dt} > 0 \\ \frac{+1}{2A_{ao}}\frac{dV(t)}{dt}, & \frac{dV(t)}{dt} < 0 \end{cases}; \end{aligned} \tag{14}$$

where A_{mv} and A_{ao} are the areas the mitral and aortic orifices, respectively. Estimations (14) are valid under the additional hypothesis of no regurgitation, either mitral or aortic.

For completeness, we can consider the y-component $U_y(t)$, which in the present approximation of vertical inflow and outflow with symmetry break limited to the x direction, is only due to the transversal motion of the wall

$$U_y(t) = \frac{1}{V(t)}\int_0^{H(t)} V_{yw}(z,t)A(z,t)dz. \tag{15}$$

The convective term $\boldsymbol{M}(t)$ in (2) can be evaluated from the knowledge of the velocity distribution on the lateral wall surface, S_{lat}, and on the basal surface. The velocity of the lateral walls is usually measurable by imaging methods and the expression of the normal vector $\boldsymbol{n}$ can also be computed from the instantaneous surface geometry to give the flux of momentum on the lateral wall.

On the valvular plane, assumed in first approximation with normal $\boldsymbol{n} = [0\ 0\ 1]$, the z-component of the velocity is approximated by

$$v_z(x,y,H,t) \approx V_z(H,t) + v_z^{(1)}(H,t)\cos\vartheta. \tag{16}$$

In the same approximation, the x-component of the velocity is given by (7) and (9)

$$v_x(x,y,H,t) \approx -\frac{r}{2}\frac{dV_z}{dz}\cos\vartheta + \left(\frac{2}{3}R - \frac{1}{2}r - \frac{1}{6}r\cos 2\vartheta\right)\frac{\partial v_z^{(1)}}{\partial z} + V_\Gamma(t), \tag{17}$$

where the last term is included to account for the circulation given by the diastolic vortex formation in the LV; this term is zero on average but is normally present at the base. Eq. (17) can be recast using (5) and (12) as

$$\begin{aligned} v_x(x,y,H,t) \approx \frac{r}{2}\frac{1}{A}\left(V_z\frac{dA}{dz} + \frac{dA}{dt}\right)\cos\vartheta + \frac{1}{A}\left(\frac{2R}{3} - \frac{r}{2} - \frac{r}{6}\cos 2\vartheta\right)\left(\frac{A}{H} - \frac{dA}{dz}\right)v_z^{(1)} \\ + \frac{\Gamma(t)}{2R}. \end{aligned} \tag{18}$$

where $\Gamma(t)$ is the vortex circulation (the vortex-induced velocity, assumed constant thorough the base, accounts for half the circulation and for its image). The circulation obeys the vortex formation process due to the roll-up of the mitral shear layer, of intensity $2v_z^{(1)}$, and a linear decay process,

$$\frac{d\Gamma}{dt} = \begin{cases} 2{v_z^{(1)}}^2 - \frac{\Gamma}{\tau}, & \frac{dV(t)}{dt} > 0 \\ 0, & \frac{dV(t)}{dt} < 0 \end{cases}; \tag{19}$$

where the dissipation decay time is taken $\tau = 0.1T$ to ensure a complete vortex dissipation within less than one third of the heartbeat in normal subjects as commonly observed. However, results were found to depend very weakly on this specific value until the order of magnitude is maintained; this decays time was introduced just to avoid the persistence of the vortex into systole. Fourier time-decomposition easily solves Eq. (19) ensuring the condition that circulation is a periodic function.

Performing the integral in (2) involving (16) and (18) provides the following

$$\boldsymbol{M}(t) = \rho\int_{S_{lat}} \boldsymbol{v}v_n dS + \rho\begin{bmatrix} V_z v_z^{(1)}\frac{R}{3}\left(\frac{A}{H} - \frac{1}{2}\frac{dA}{dz}\right) + \frac{R}{6}\frac{dA}{dt}v_z^{(1)} + V_z V_{xw}A + V_z\Gamma(t)\frac{A}{4R} \\ V_z V_{yw}A \\ \left(V_z^2 + \frac{1}{2}{v_z^{(1)}}^2\right)A. \end{bmatrix}; \tag{20}$$

where the first term on the right hand side is the flux of momentum on the lateral wall and the second terms represent that through the base with all quantities therein evaluated at the valvular level.

4. Results

The time profiles of the hemodynamic force (measured in Newton) evaluated from PC-MRI and estimated from the mathematical model are visually compared for each subject in Figs. 3 and 4 for the base-apex and the inferolateral-anteroseptal components, respectively. Table 2 reports the correlation coefficients between the time profiles which measures the similarity in the time fluctuations. Here, a small displacement of max ±1 time interval between two frames was allowed to improve alignment of the profiles accounting for the different time resolution between PC-MRI, used to compute the force, and bSSFP cine images from which endocardial borders are extracted. It should also be remarked that the two recordings were not simultaneous and the heartbeat rate can vary between the two, as shown in Table 1; some further differences can be imputable to the different segmentation of the cavity that is made of parallel short axis slices in MRI while the model combines the 3 long axis borders. The model reproduces the main features of the longitudinal forces, shown in Fig. 3, in terms of amplitude and time profile with correlation coefficients above 0.7 for most subjects. Similarity is lower for the anteroseptal-inferolateral component of the force, shown in Fig. 4, the main time variations are only partly followed although it is important to notice how the model captures the relative entity of the force component, which is highly variable among subjects. The third force

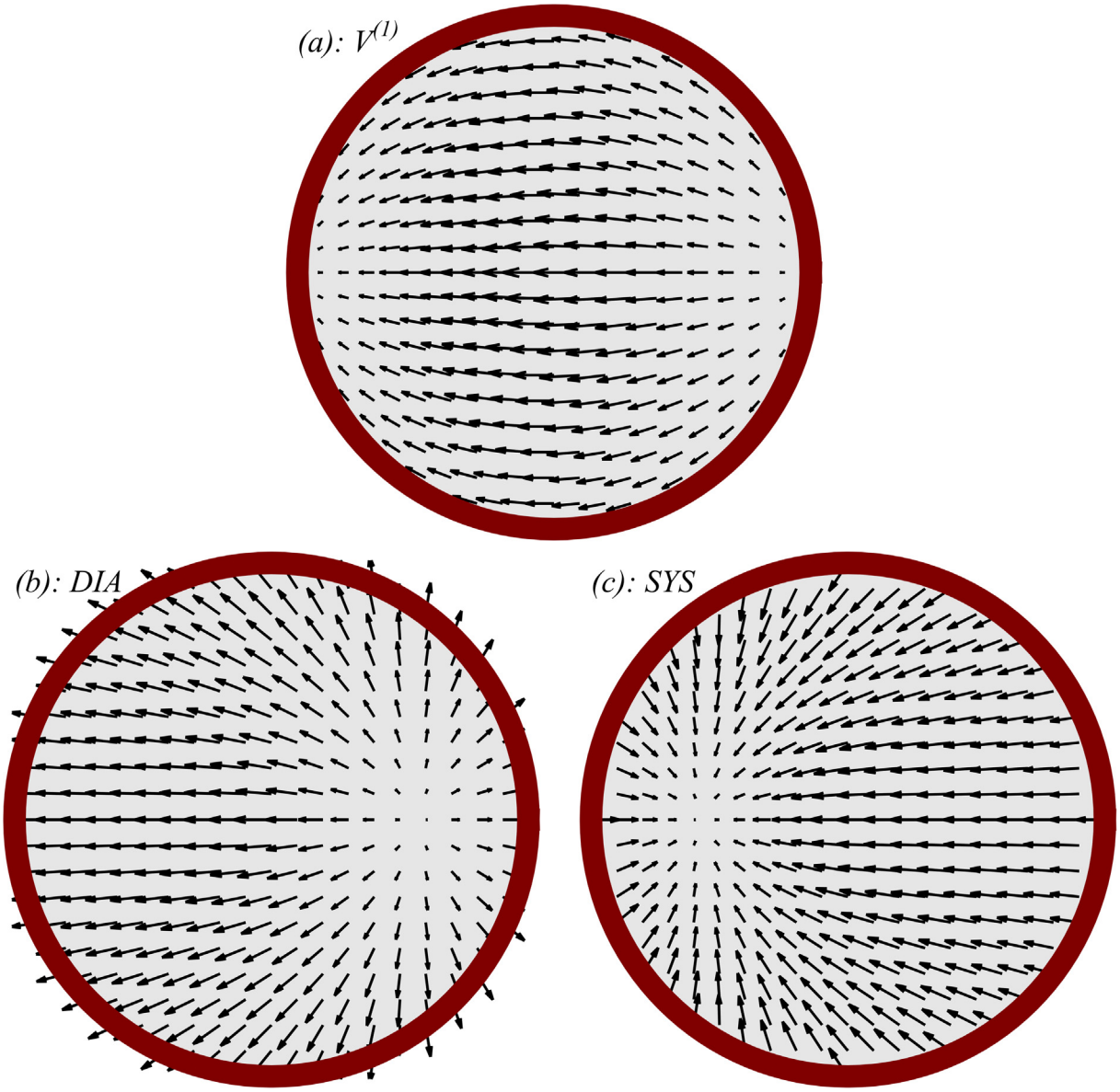

Fig. 2. Velocity vector field on the transversal plane as assumed in the mathematical model. (a) The additional flow field corresponding to the asymmetric component of the longitudinal velocity; (b) the same field added to an outward radial velocity due to diastolic LV widening and (c) added to an inward radial velocity as expected during systolic LV contraction.

component (not shown in the graphs) is largely underestimated and was included in the model for completeness only. This component is primarily caused by details of LV structural orientation at the inflow and outflow tracts that break the left-right symmetry hypothesized here.

An integrated quantitative comparison of the force amplitude is given in Fig. 5 that reports the root mean square (RMS) values of the longitudinal and transversal force components. The correlations between measured and estimated values are evaluated by a direct linear fit of the type $y = ax$; figures confirm that the model provides a good correlation ($r = 0.88$) and non-biased (best fit: $y = 0.98x$) estimation of the overall longitudinal force entity. The correlation is good for the transversal force as well ($r = 0.84$), although the model gives a small underestimation of the RMS value (best fit: $y = 0.87x$).

5. Discussion

Hemodynamic forces, or IVPGs, drive blood motion during both ventricular ejection and ventricular filling. They represent the ultimate result of LV deformation and play a central role in cardiac function that governs blood flow. Moreover, flow-mediated forces influence cardiomyocyte hypertrophy and ventricular chamber enlargement and, therefore, participate to cardiac adaptation (Andrés-Delgado and Mercader, 2016; Pasipoularides, 2015; Pedrizzetti et al., 2014). Despite their potential relevance, hemodynamic forces are not part of the clinical diagnostic process due to the complexity of their acquisition. This study introduces a method for estimating hemodynamic forces, or IVPGs, without the need of measuring blood flow, from the motion of the LV endocardial boundary, which can be valuated non-invasively in both cardiac MRI and echocardiography.

Non-invasive measurement of IVPGs was previously proposed in echocardiography by post-processing of M-mode color Doppler (Bermejo et al., 2001; Firstenberg et al., 2000; Greenberg et al., 2001; Tonti et al., 2001). That approach, which integrated the Euler equation along the ultrasound beam assumed as a flow streamline, has not seen widespread use. One reason could be its limitation of evaluating along one single line with just one velocity component. Another reason could be imputable to reliability of color Doppler for quantification, or simply the availability of quantification tools. More recently, hemodynamic forces were evaluated by Echo-PIV (Pedrizzetti et al., 2016, 2015). Echo-PIV presents several limitations in accuracy that make it more appropriate for detecting changes in the same patient over time than it is for absolute measurements. The need of infusion a contrast agent also complicates its application. PC-MRI represents the most generally reliable tool for measuring blood velocities and hemodynamic forces in the heart (Arvidsson et al., 2016b; Eriksson et al., 2016). It presents a limitation in terms of time resolution, which can be important for computing the inertial term, and by the fact that recording is an average over numerous heartbeats. Nevertheless, PC-MRI is the reference standard for measuring multidimensional blood motion. This is why it was used for the validation of the present method.

In clinical applications, only the time profile of longitudinal (base-apex) IVPGs were considered so far (Courtois et al., 1988; Guerra et al., 2013a,b). The force component along the inferolateral-anteroseptal direction was considered only in terms of its entity relative to the longitudinal leading to misalignment between IVPGs and LV axis (Cicchitti et al., 2016; Pedrizzetti et al., 2016). The present model for the longitudinal force is relatively straightforward and based on first physical principles. Differently, assumptions about intraventricular flow was necessarily introduced for drawing transversal balances, ignoring intraventricular vortex instabilities and assuming mitral jet and the aortic outflow aligned with the LV axis. These assumptions limit the accuracy in estimating transversal force; nevertheless, some mean properties, like the variations of amplitude among subjects are still captured with good correlation.

It is worth mentioning that 4D flow and bSSFP recordings were not simultaneous and may present some differences, which is more likely in unstable patients as well as in cases presenting different heartbeat periods (T_{SSFP} and T_{4DFlow} in Table 1), that would reduce the comparability. The current findings suggest that minor differences between subsequent recordings influence the time profile of the transversal force more than the longitudinal, although they do not affect much the force amplitude or RMS.

The model introduced here allows quantification of hemodynamic forces using routine clinically used scans, instead of time-consuming flow measurements requiring advanced post-processing. It may represent a potential integration to the existing methods of quantifying deformation in cardiac imaging. The endocardial borders, evaluated by MRI feature tracking or echocardiographic speckle tracking, could be used directly as input to the

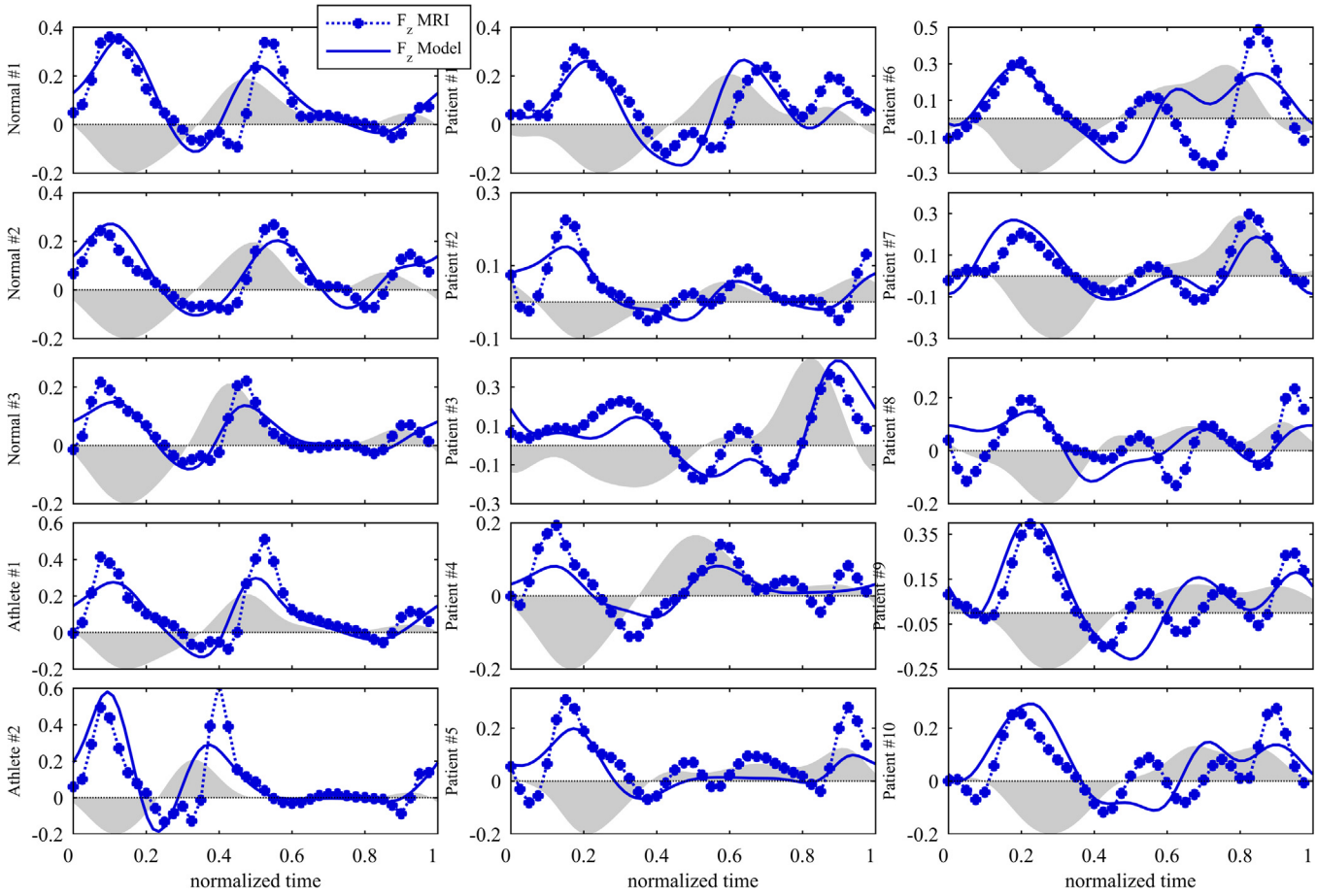

Fig. 3. Time profiles of the apex-base force component for all 15 individual subjects as measured by PC-MRI (dotted line with dots) and estimated by the mathematical model (continuous line). For timing reference, the shaded profile shows (not in scale) the time course of dV/dt.

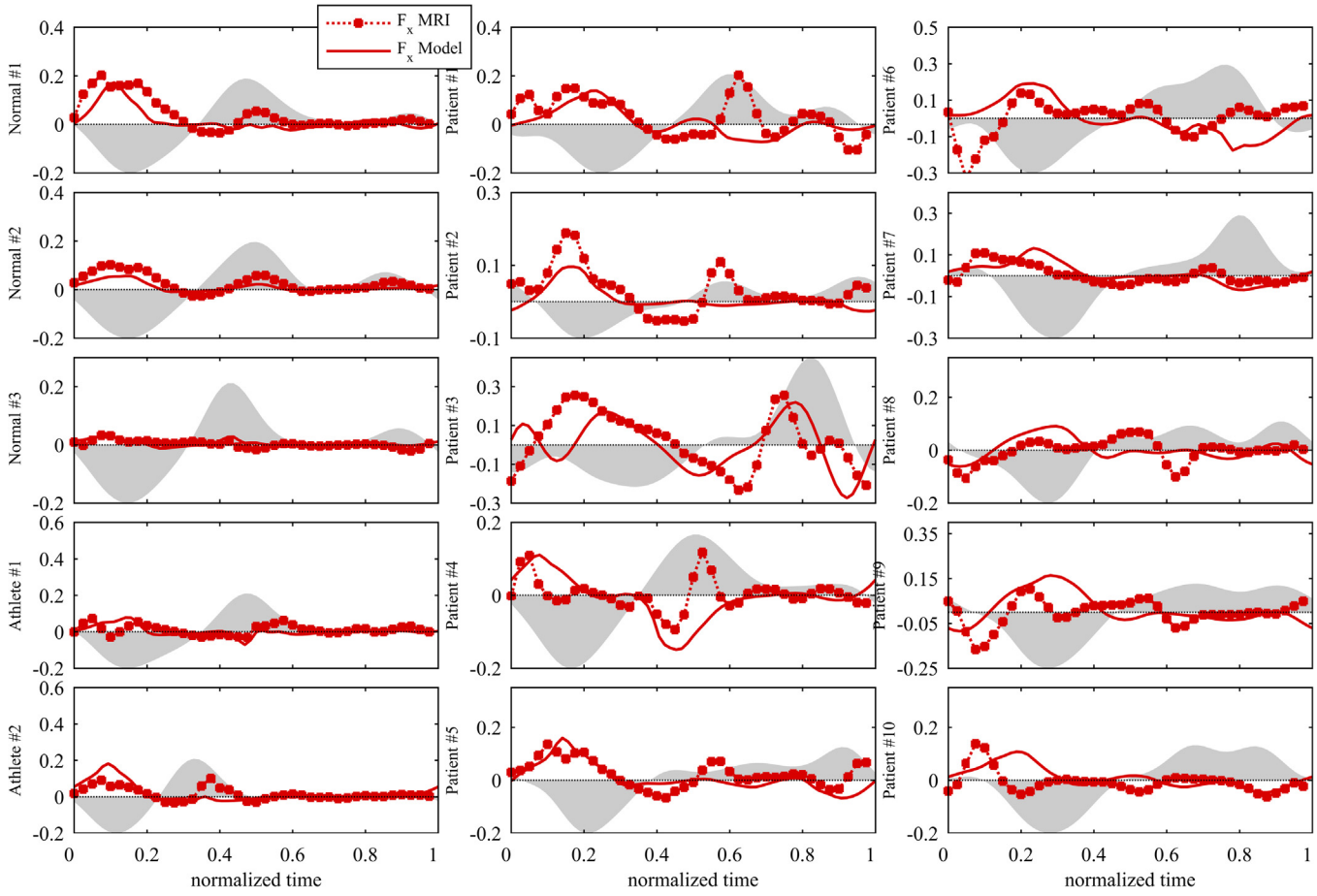

Fig. 4. Time profiles of the inferolateral-anteroseptal force component for all 15 individual subjects as measured by PC-MRI (dotted line with dots) and estimated by the mathematical model (continuous line). Scale limits are maintained as in Fig. 3 for comparison. For timing reference, the shaded profile shows (not in scale) the time course of dV/dt.

Table 2
Coefficient of correlation between the instantaneous values of hemodynamic force estimated by the model and measured by MRI for individual subjects.

#		Base-Apex	Inferolateral-Anteroseptal
1	Normal #1	0.856	0.825
2	Normal #2	0.897	0.927
3	Normal #3	0.871	0.497
4	Athlete #1	0.843	0.314
5	Athlete #2	0.769	0.632
6	Patient #1	0.767	0.374
7	Patient #2	0.764	0.695
8	Patient #3	0.841	0.485
9	Patient #4	0.870	0.380
10	Patient #5	0.732	0.702
11	Patient #6	0.559	0.230
12	Patient #7	0.810	0.638
13	Patient #8	0.486	0.345
14	Patient #9	0.767	0.277
15	Patient #10	0.678	0.210
	Mean ± St.Dev.	0.77 ± 0.12	0.50 ± 0.22

present model to provide a non-invasive assessment of hemodynamic forces.

Conflict of interest

All authors declare no conflicts of interest, financial or otherwise.

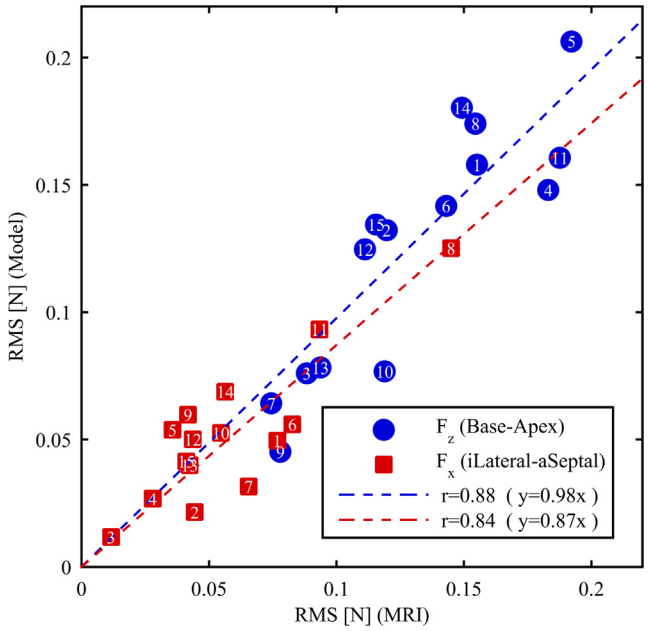

Fig. 5. Relationship between the RMS of the longitudinal and transversal force components measured by PC-MRI and estimated by the mathematical model. The number inside the symbols represent the subject number. The correlation coefficients and the parameters of the linear fit are reported on the bottom-right for the two components.

Acknowledgements

GP was supported by the University of Trieste. FD was supported by the University of Firenze. The authors in Lund were supported by Region of Scania, Swedish Heart and Lung Foundation, and Swedish Research Council.

Appendix A. Supplementary material

Supplementary data associated with this article can be found, in the online version, at http://dx.doi.org/10.1016/j.jbiomech.2017.06.046.

References

Andrés-Delgado, L., Mercader, N., 2016. Interplay between cardiac function and heart development. Biochim. Biophys. Acta – Mol. Cell Res. 1863, 1707–1716. http://dx.doi.org/10.1016/j.bbamcr.2016.03.004.

Arvidsson, P.M., Kovács, S.J., Töger, J., Borgquist, R., Heiberg, E., Carlsson, M., Arheden, H., 2016a. Vortex ring behavior provides the epigenetic blueprint for the human heart. Sci. Rep. 6, 22021. http://dx.doi.org/10.1038/srep22021.

Arvidsson, P.M., Töger, J., Carlsson, M., Steding-Ehrenborg, K., Pedrizzetti, G., Heiberg, E., Arheden, H., 2016b. Left and right ventricular hemodynamic forces in healthy volunteers and elite athletes assessed with 4D flow magnetic resonance imaging. Am. J. Physiol. – Hear. Circ. Physiol. http://dx.doi.org/10.1152/ajpheart.00583.2016.

Bermejo, J., Antoranz, J.C., Yotti, R., Moreno, M., García-Fernández, M.A., 2001. Spatio-temporal mapping of intracardiac pressure gradients. A solution to Euler's equation from digital postprocessing of color Doppler M-mode echocardiograms. Ultrasound Med. Biol. 27, 621–630. http://dx.doi.org/10.1016/S0301-5629(01)00349-0.

Bogaert, J., Rademakers, F.E., 2001. Regional nonuniformity of normal adult human left ventricle. Am. J. Physiol. Hear. Circ. Physiol. 280, H610–20.

Carlsson, M., Andersson, R., Bloch, K.M., Steding-Ehrenborg, K., Mosén, H., Stahlberg, F., Ekmehag, B., Arheden, H., 2012. Cardiac output and cardiac index measured with cardiovascular magnetic resonance in healthy subjects, elite athletes and patients with congestive heart failure. J. Cardiovasc. Magn. Reson. 14, 51. http://dx.doi.org/10.1186/1532-429X-14-51.

Cicchitti, V., Radico, F., Bianco, F., Gallina, S., Tonti, G., De Caterina, R., 2016. Heart failure due to right ventricular apical pacing: the importance of flow patterns. Europace 1679–1688. http://dx.doi.org/10.1093/europace/euw024.

Cimino, S., Pedrizzetti, G., Tonti, G., Canali, E., Petronilli, V., De Luca, L., Iacoboni, C., Agati, L., 2012. In vivo analysis of intraventricular fluid dynamics in healthy hearts. Eur. J. Mech. B/Fluids 35, 40–46. http://dx.doi.org/10.1016/j.euromechflu.2012.03.014.

Claus, P., Omar, A.M.S., Pedrizzetti, G., Sengupta, P.P., Nagel, E., 2015. Tissue tracking technology for assessing cardiac mechanics: principles, normal values, and clinical applications. JACC Cardiovasc. Imag. 8, 1444–1460. http://dx.doi.org/10.1016/j.jcmg.2015.11.001.

Courtois, M., Kovács, S.J., Ludbrook, P.A., 1988. Transmitral pressure-flow velocity relation. Importance of regional pressure gradients in the left ventricle during diastole. Circulation 78, 661–671. http://dx.doi.org/10.1161/01.cir.78.3.661.

Domenichini, F., Pedrizzetti, G., 2016. Hemodynamic forces in a model left ventricle. Phys. Rev. Fluids. http://dx.doi.org/10.1103/PhysRevFluids.00.003200.

Ebbers, T., Wigstrm, L., Bolger, A.F., Engvall, J., Karlsson, M., 2001. Estimation of relative cardiovascular pressures using time-resolved three-dimensional phase contrast MRI. Magn. Reson. Med. 45, 872–879. http://dx.doi.org/10.1002/mrm.1116.

Eriksson, J., Bolger, A.F., Ebbers, T., Carlhäll, C.-J., 2016. Assessment of left ventricular hemodynamic forces in healthy subjects and patients with dilated cardiomyopathy using 4D flow MRI. Physiol. Rep. 4, 741–747. http://dx.doi.org/10.14814/phy2.12685.

Firstenberg, M.S., Vandervoort, P.M., Greenberg, N.L., Smedira, N.G., McCarthy, P.M., Garcia, M.J., Thomas, J.D., 2000. Noninvasive estimation of transmitral pressure drop across the normal mitral valve in humans: importance of convective and inertial forces during left ventricular filling. J. Am. Coll. Cardiol. 36, 1942–1949. http://dx.doi.org/10.1016/S0735-1097(00)00963-3.

Greenberg, N.L., Vandervoort, P.M., Firstenberg, M.S., Garcia, M.J., Thomas, J.D., 2001. Estimation of diastolic intraventricular pressure gradients by Doppler M-mode echocardiography. Am. J. Physiol. Heart Circ. Physiol. 280, H2507–15.

Guerra, M., Amorim, M.J., Brás-Silva, C., Leite-Moreira, A.F., 2013a. Intraventricular pressure gradients throughout the cardiac cycle: effects of ischaemia and modulation by afterload. Exp. Physiol. 98, 149–160. http://dx.doi.org/10.1113/expphysiol.2012.066324.

Guerra, M., Brás-Silva, C., Amorim, M.J., Moura, C., Bastos, P., Leite-Moreira, A.F., 2013b. Intraventricular pressure gradients in heart failure. Physiol. Res. 62, 479–487.

Heiberg, E., Sjögren, J., Ugander, M., Carlsson, M., Engblom, H., Arheden, H., 2010. Design and validation of Segment – freely available software for cardiovascular image analysis. BMC Med. Imag 10, 1. http://dx.doi.org/10.1186/1471-2342-10-1.

Kanski, M., Töger, J., Steding-Ehrenborg, K., Xanthis, C., Bloch, K.M., Heiberg, E., Carlsson, M., Arheden, H., 2015. Whole-heart four-dimensional flow can be acquired with preserved quality without respiratory gating, facilitating clinical use: a head-to-head comparison. BMC Med. Imag. 15, 20. http://dx.doi.org/10.1186/s12880-015-0061-4.

Kawel-Boehm, N., Maceira, A., Valsangiacomo-Buechel, E.R., Vogel-Claussen, J., Turkbey, E.B., Williams, R., Plein, S., Tee, M., Eng, J., Bluemke, D.A., 2015. Normal values for cardiovascular magnetic resonance in adults and children. J. Cardiovasc. Magn. Reson. 17, 29. http://dx.doi.org/10.1186/s12968-015-0111-7.

Maffessanti, F., Lang, R.M., Niel, J., Steringer-mascherbauer, R., Caiani, E.G., Nesser, H., Mor-avi, V., 2011. Three-dimensional analysis of regional left ventricular endocardial curvature from cardiac magnetic resonance images. Magn. Reson. Imag. 29, 516–524. http://dx.doi.org/10.1016/j.mri.2010.11.002.

Pasipoularides, A., 2015. Mechanotransduction mechanisms for intraventricular diastolic vortex forces and myocardial deformations: Part 1. J. Cardiovasc. Transl. Res. 8, 76–87. http://dx.doi.org/10.1007/s12265-015-9611-y.

Pedrizzetti, G., La Canna, G., Alfieri, O., Tonti, G., 2014. The vortex—an early predictor of cardiovascular outcome? Nat. Rev. Cardiol. 11, 545–553. http://dx.doi.org/10.1038/nrcardio.2014.75.

Pedrizzetti, G., Martiniello, A.R., Bianchi, V., D'Onofrio, A., Caso, P., Tonti, G., 2016. Changes in electrical activation modify the orientation of left ventricular flow momentum: novel observations using echocardiographic particle image velocimetry. Eur. Heart J. Cardiovasc. Imag. 17, 203–209. http://dx.doi.org/10.1093/ehjci/jev137.

Pedrizzetti, G., Martiniello, A.R., Bianchi, V., D'Onofrio, A., Caso, P., Tonti, G., 2015. Cardiac fluid dynamics anticipates heart adaptation. J. Biomech. 48, 388–391. http://dx.doi.org/10.1016/j.jbiomech.2014.11.049.

Richter, Y., Edelman, E.R., 2006. Cardiology is flow. Circulation 113, 2679–2682. http://dx.doi.org/10.1161/CIRCULATIONAHA.106.632687.

Shah, A.M., Solomon, S.D., 2012. Myocardial deformation imaging: current status and future directions. Circulation 125. http://dx.doi.org/10.1161/CIRCULATIONAHA.111.086348.

Steding, K., Engblom, H., Buhre, T., Carlsson, M., Mosén, H., Wohlfart, B., Arheden, H., 2010. Relation between cardiac dimensions and peak oxygen uptake. J. Cardiovasc. Magn. Reson. 12, 8. http://dx.doi.org/10.1186/1532-429X-12-8.

Töger, J., Arvidsson, P.M., Kanski, M., Steding-Ehrenborg, K., Pedrizzetti, G., Carlsson, M., Arheden, H., Heiberg, E., 2016. Intracardiac hemodynamic forces using 4D flow: a new reproducible method applied to healthy controls, elite athletes and heart failure patients. J. Cardiovasc. Magn. Reson. 18, 1–3.

Tonti, G., Pedrizzetti, G., Trambaiolo, P., Salustri, A., 2001. Space and time dependency of inertial and convective contribution to the transmitral pressure drop during ventricular filling. J. Am. Coll. Cardiol. 38, 290–291.

Tufvesson, J., Hedström, E., Steding-Ehrenborg, K., Carlsson, M., Arheden, H., Heiberg, E., 2015. Validation and development of a new automatic algorithm for time-resolved segmentation of the left ventricle in magnetic resonance imaging. Biomed. Res. Int. 2015, 1–12. http://dx.doi.org/10.1155/2015/970357.